14

Photoconductors for Measuring Speckle Motion to Monitor Ultrasonic Vibrations

Jonathan Bessette and Elsa Garmire
Dartmouth College
USA

1. Introduction

This chapter explains a unique miniature photoconductive detector design that has been specifically engineered with a speckle-monitoring application in mind. Small arrays of these detectors have been fabricated with silicon-on-insulator (SOI) technology and in semi-insulating GaAs, and have been put to work measuring surface vibrations in laboratory experiments. The important characteristics of these photodetectors are their small physical dimensions, on the order of 10 μm, with an ability to measure ultrasonic bandwidths extending into the megahertz regime, and with high internal gain. The advantage of photo-conductors is their capability of generating multiple electrons of photocurrent for each photon captured.[1]

2. Performance of a general photodetector

At the most fundamental level, electronic photodetection is a method of counting photons by converting them into some form of electronic current. There are many ways to do this, including all the familiar detector technologies such as photodiodes, photomultiplier tubes, and photoconductors, to name a few. For the purposes of this discussion, all these detectors can be abstracted into a simple detector model consisting of three primary parameters: gain, noise, and bandwidth.

Gain can be neatly expressed as the number of electrons per unit time of signal current either generated or modulated by the detector divided by the number of photons per unit time incident upon it. A gain of one, for example, indicates that one electron flows for every photon collected.

Noise is a measure of the electronic current generated or modulated due to random fluctuations in either the arrival or conversion rate of photons, or due to the random generation of the flow of electrons within the detection circuit not caused by photons at all.

Bandwidth is a measure of the maximum frequency response of the detector to a photonic signal. The higher the bandwidth, the faster the detector can respond to changes in the level

[1] Much of this chapter comes from the PhD thesis of Jon Bessette: "Silicon-on-Insulator Photoconducting Mesas For High-Speed Laser Speckle Monitoring Applications," Dartmouth College, June, 2010.

of illumination. Bandwidth limits may be imposed by the internal physics of the device or additionally by a combination of factors in the circuit implementation.

Gain, noise, and bandwidth are always intimately connected in any detection system and improved performance in one parameter often comes at the price of decreased performance in another. It is important therefore to understand the connections between them for any given detector technology and the detector application.

A simple model combines these three elements into a description of the signal from a generic photodetector in the useful form of a signal-to-noise ratio (SNR). This ratio indicates a lower bound of sensitivity for which a detector is useful in a given operating regime. The convention adopted here is to express the SNR as the ratio of signal power to noise power:

$$SNR_{gen} = \frac{(e\Gamma A \Delta I)^2}{\sigma^2_{noise}(\Gamma, B)} \tag{1}$$

The numerator is given in units of current squared, where e is the electron charge, Γ is the detector gain, A is the detector area, and ΔI is the change in optical intensity incident on the detector during the time $2/B$. The noise term σ^2 is expressed in units of current squared and is generally a function of the gain Γ, bandwidth B, and the specifics of the detector. There are multiple sources of noise in the signal of any detector that measures changes in incident optical power. The predominant forms of noise in the simple model presented here are photon shot noise, current shot noise, and circuit thermal noise. These noise sources are all well understood and characterized by circuit designers and so will only be summarized here:

- Photon shot noise is caused by the random arrival of discrete photons in a given photon stream. The power in the photon shot noise is proportional to the average incident optical power, and the variance can be given in units of current as $\sigma^2_\varphi = 2e^2\Gamma^2 FAI_o B/h\nu$, where F is an excess noise factor created by probabilistic gain mechanisms and I is the intensity incident on the detector (Liu, 2005).
- Current shot noise is caused by the random arrival of discrete electrons in a given electric current. Its power is proportional to the average background current i and its variance is given as $\sigma_i^2 = 2ei\Gamma^2 FB$.
- Circuit thermal noise is created by random thermal motion of the electrons in a conductor. It is independent of the current flowing through the load resistor R_L and is present even when no electric potential is applied. The thermal noise variance is approximately $\sigma_K^2 = 4k_B TB/R_L$.

In general, the different noise sources are assumed to be independent of each other. This means that the variance of the combined noise amplitude is the sum of the variances of the individual noise sources, i.e. $\sigma_{noise}^2 = \sigma_\varphi^2 + \sigma_i^2 + \sigma_K^2$. To quantify the expected performance of a given detector in a particular operating regime, we must explore the magnitude of the various gain and noise terms for different classes of detectors. Because rather small area detectors are required for our application, we will restrict ourselves to the discussion of semiconductor-based detectors. These can be manufactured on the appropriate scales and easily configured for array operation, which can greatly enhance their effectiveness.

2.1 Gain and noise

The fundamental operating principle of all solid-state photosensitive devices is the same. A photon with sufficient energy interacts with a semiconductor crystal, temporarily changing the distribution of electron energies within the crystal. One electron gains enough energy to attain an energetic conductive state, where it is free to move about within the crystal. The promoted electron leaves behind a vacancy, called a hole, which can also move about within the crystal. Together, these are referred to as an electron-hole pair, and in an ideal photodetector, one such pair is created for every absorbed photon. Eventually, if left in the crystal long enough, the electron-hole pair will recombine, giving up the extra energy in the form of heat. This happens on a characteristic time scale called the recombination lifetime, τ_r.

While excited, the electron and hole will drift in the presence of an electric field, creating an electric current. This current can be detected by connecting the active area of the semiconductor into an electronic circuit. How the electric field is applied and the nature of the electrical contacts defines the class of detector.

2.1.1 Photoconductors

Photoconductors are uniformly doped semiconductors whose conductance changes in proportion to the number of photons absorbed per unit time. When an electrical potential is placed across the photoconductor, the amount of current flowing through the photoconductor indicates the amount of light incident on it. The photoconductor is perhaps the simplest kind of semiconductor photodetector. It is perhaps surprising, then, that such a simple device may exhibit internal gain.

The photoconductor gain is the ratio of electron collection at the contacts to electron-hole pair generation by photons within the channel. The gain is the ratio of recombination time to the average transit time of charge carriers across the photoconductive channel. This ratio is, in turn, determined (at low applied voltages) by the photoconductor's effective combined carrier mobility $\mu = (\mu_e + \mu_h)$, its carrier recombination time τ_r, its channel length L and the applied voltage V according to

$$\Gamma = V\mu\tau/L^2 \tag{2}$$

(for a square detector, $\Gamma = V\mu\tau/A$ where A is area). This gain process is fundamentally probabilistic for each individual photon absorbed, and so necessarily the mechanism produces an excess noise factor. The excess noise factor for a uniformly illuminated photoconductor with such a gain, governed by Poisson statistics of a uniform random variable, is 2 (Liu, 2005).

It is important to note that the gain does not scale linearly with voltage indefinitely. At least two effects may limit the maximum gain seen inside a photoconductive element. The first of these is drift velocity saturation, which occurs when the electric field is great enough to yield carrier drift velocities on the order of the carrier thermal velocity. Increasing the electric field beyond this saturation value - about 30 kV/cm for silicon - does not cause the carriers to drift any faster (Neamen, 2004). Consequently, the transit time is not reduced with greater field strength and gain saturates.

A second mechanism that limits the internal gain is space-charge current limitation (Liu, 2005; Bube, 1960; Rose 1958), when charges build up on either electrode due to the effective

capacitance of the device. When this charge exceeds the total number of free carriers within the photoconductor, the excess charge is injected into the device and carries a current that is limited by the dielectric relaxation of the capacitor (Rose, 1954). These so-called space-charge currents screen the photogenerated carriers from any additional electric field, so that increasing the applied potential difference beyond a certain threshold does not increase the photocurrent, and the gain saturates.

The threshold voltage that limits the gain is called the space-charge voltage. It is equal to the applied potential that causes the charge on the effective capacitor to exceed the number of free carriers within the photoconductive channel. For a photoconductor with ohmic contacts and charge carriers of both sign, this is explicitly

$$V_{SC} = \frac{\oint(\sigma_0 + \sigma_{ph})\mathbf{dv}}{e\mu C} \tag{3}$$

where σ_0 is the dark conductivity, σ_{ph} is the photogenerated conductivity, and the integral is over the volume of the photoconductor. The value given for capacitance depends on the exact geometry and material properties of the photoconductor, but for the simplest model of parallel electrodes and a block-shaped semiconductor, the capacitance is simply $C = WD\varepsilon/L$ and the space-charge voltage is (Liu, 2005)

$$V_{SC} = \frac{(\sigma_0 + \sigma_{ph})L^2}{\epsilon\mu}. \tag{4}$$

The gain limit for a space-charge limited device becomes

$$\Gamma_{max} = \frac{\tau(\sigma_0 + \sigma_{ph})}{\epsilon}. \tag{5}$$

Note that the gain limit is a function of photoconductivity (i.e., depends on the amount of light being absorbed), but that this does not greatly affect the performance unless the photoconductivity is comparable to the dark current.

For the dimensions and material of devices investigated in this chapter, it is not the saturation velocity limit but rather the space-charge current that limits the photoconductive gain.

As far as noise is concerned, the dark current shot noise of a photoconductor can be significant in certain operating regimes. For an ideal photoconductor, this noise figure scales linearly with the applied voltage and the cross-sectional area-to-length ratio of the active region. This can be deduced by plugging in the ideal photoconductor dark current into the definition of shot noise

$$\sigma_{i,d}^2 = 2eV\frac{WD}{\rho_0 L}B, \tag{6}$$

where σ_0 is the dark resistivity of the photoconductor. We will see in a following section that this noise figure is dominated by the circuit thermal noise at high bandwidths.

2.1.2 Photodiodes

Photodiodes are rectifying junctions created by adjoining two regions of a semiconductor crystal that are doped with different impurities. The impurities change the equilibrium concentrations of conductive electrons and holes. When a semiconductor is *p*-doped, it has an excess of mobile positive charges (holes). Likewise when it is *n*-doped, the semiconductor has an excess of negative charges (electrons). Note that the total charge of the crystal remains neutral - this implies there are fixed negative charges in the *p*-doped regions and fixed positive charges in the *n*-doped regions.

When two regions of opposite doping are brought into contact, diffusion results in excess mobile charges from each region spreading into the neighboring region, leaving behind some fixed charge. The fixed charge is of opposite polarity on either side of the junction and together the two zones are called the space-charge region.

The space-charge region supports an electric field which points from the *n*-doped side of the junction to the *p*-doped side of the junction. When a photon is absorbed in this region, the resulting electron and hole are quickly swept out through opposite contacts as a result of the electric field. Reverse-bias is generally applied, which means a relatively positive potential is placed on the *n*-doped side of the junction. This widens the junction and increases the maximum field in the space-charge region.

Once mobilized by the absorption of the photon, the electron drifts toward the (positively charged) *n*-doped side of the space-charge region and the hole toward the (negatively charged) *p*-doped side of contact, and the circuit registers a blip of electric current. Once the carriers reach the end of the space charge region, they eventually recombine.

In contrast to the ohmic photoconductor contacts, the *pn* junction barrier under reverse bias acts as a completely blocking contact for the drift of both charge carriers, so that no additional carriers are injected into the space-charge region. Since the photo-induced charge only transits the active region once, the photodiode produces only one unit of electronic current for every photon absorbed. The basic photodiode thus has a maximum of unity internal gain.

The dark current is generally very low for most photodiodes, on the order of pico-amperes for small diodes, and it only decreases as the detector area is reduced. Consequently, the dark current noise is dominated at higher bandwidths by the circuit thermal noise.

2.1.3 Metal-semiconductor-metal photodiodes

Metal-semiconductor-metal photodiodes are created by making contact with a semiconductor using a metal that forms a Schottky potential barrier. Each metal-semiconductor junction exhibits the rectifying properties of a diode. Charge carriers diffuse across the junction to establish a space-charge layer at each contact, similar to *pn* junction diodes. However, unlike *pn* diodes, the current across the Schottky junction barrier is carried by the drift of semiconductor majority-charge carriers and not minority carrier diffusion.

When a bias is placed across the contacts, one of the junctions is forward-biased and one is reverse-biased. It is the reverse-biased contact that limits the current in the rectifying regime.

Another distinction that separates MSM photodiodes from *pn* junction diodes is that they can exhibit photoconductive gain greater than unity, despite the non-ohmic contacts and rectifying Schottky barriers. The source of this gain is the same mechanism as for photoconductors, namely multiple charge carriers make a transit across the semiconductor region for every photon absorbed, despite the presence of the Schottky barriers at the contacts. This is possible because carriers can be injected via thermionic emission over the Schottky barrier (Neamen, 2003; Soares, 1992; Burm, 1996) to maintain charge neutrality. That is to say, the Schottky barrier is not a completely blocking contact - it merely presents an additional potential barrier that increases the device resistance. This is a key difference between *pn* junction photodiodes and Schottky barrier photodiodes.

The dark current in MSM photodiodes can be many orders of magnitude greater than the dark current in reverse-biased photodiodes. Consequently, the dark current noise in MSM photodiodes is of greater concern. The dark current can be estimated by the following formula for the reverse-bias saturation current density in units of current per cross-sectional area (Neamen, 2003):

$$J_{sT} = A^* T^2 \exp\left(\frac{-e\Phi_B}{k_B T}\right) \tag{7}$$

where A^* is called the Richardson constant with units of $AK^{-2}cm^{-2}$ (A is amperes) and is specific to the semiconductor, T is temperature in Kelvin, and Φ_B is the Schottky barrier height in units of eV.

As an example, consider a silicon Schottky diode with chromium contacts, similar to the SOI prototype construction discussed later in this chapter. The Richardson constant for silicon is approximately $A^* = 114\ AK^{-2}cm^{-2}$ and the barrier height is approximately 0.49 V. Thus, at room temperature, the reverse saturation (dark) current is approximately $J_{sT} \approx (114\ AK^{-2}cm^{-2}) \times (300\ K)^2 \times \exp(-0.49\ eV/0.026\ eV) = 67\ mA/cm^2$. For a cross sectional area of 10 μm × 10 μm, this gives about 67 nA of dark current, which has a significant impact on noise at low bandwidths.

It should be noted that the Schottky barrier height can be a significant function of both the applied voltage and the level of illumination. This occurs through several mechanisms, including image force lowering (the Schottky effect), (Neamen, 2003; Soares, 1992) charge tunneling from the metal across the barrier (Soares, 1992), and photogenerated charge accumulation (Soares, 1992; Carrano, 1998). By these processes, charges are pulled to either contact where they establish compensating electric fields. The effect is to lower the potential barrier with additional applied voltage and consequently modify the current-voltage characteristics of the diode - as the reverse bias voltage increases, so does the reverse saturation current.

2.2 Small area detectors in the thermal noise limit

By way of example, let us compare the predicted performance of photoconductors and photodiodes in the face of noise for a megahertz bandwidth and low detector area situation. The parasitic capacitance for both photodiodes and photoconductors for small detectors is usually somewhere in the 10 pF range or greater. If we want to operate with a 1 MHz

bandwidth, we require an RC time constant such that R_LC = 1/(2π×1MHz) = 160 ns. This means we need to use a load resistance no greater than RL = 16 Ω, and the thermal noise generated by such a load at room temperature T will be

$$\sigma_K = \sqrt{4k_BTB/R_L} \approx 1\ \text{nA} \tag{8}$$

This noise figure is quite significant and dominates the other primary sources of noise, photon shot noise and dark current noise. Take the photon shot noise for example. A detector with an active area of 100 μm^2 under 1 mW/cm^2 illumination sees a total of 1 nW optical power P_0. At an optical wavelength of 1 μm, this corresponds to a photon shot noise of

$$\sigma_\Phi = (\sqrt{2P_0F/h\nu})e\Gamma B \approx \Gamma \times 10\ \text{pA}.$$

This is less than thermal noise for gains less than 100.

The dark current noise is often negligible as well. For small area photodiodes, the dark current itself is negligible compared to the thermal noise. (Consider that the dark current scales with detector area and 1 mm^2 detectors have dark currents in the pA range.) Photoconductors have considerably more dark current, but in most cases the noise associated with it will not be more significant than the thermal noise. For instance, according to Eq. 6, the dark current noise of an ideal photoconductor with a dark resistivity of 10 kΩ-cm that is 10 μm thick, 10 μm wide and 10 μm long, and operated with 1 V applied at 1 MHz bandwidth is

$$\sigma_{i,d} = \sqrt{2eVWDB/\rho_0L} \approx 200\ \text{pA}$$

This is still less than the thermal noise, even for the highest allowable resistor load.

If we examine the SNR for photoconductors and photodiodes using the above approximations and Eq. 1, we obtain

$$SNR = \frac{(e\Gamma A\Delta I)^2}{4k_BT/R_L} \tag{9}$$

where the gain Γ_{pd} = 1 for photodiodes and the gain Γ_{pc} is a function of geometry and applied voltage for photoconductors. In this approximation, the SNR scales with the square of the internal gain. This implies that the performance of a photoconductor will exceed the performance of a photodiode whenever the gain is greater than one.

In Fig. 1, a direct comparison between the SNR for photoconductors and photodiodes is plotted as a function of detector area, WD, assuming a square detector, load resistance of RL = 1 kΩ, a bandwidth of B = 1 MHz, a photoconductor recombination time τ_R = 10 ns, a photoconductor mobility of 1850 cm^2=V•s, and an applied photo-conductor voltage of 1 V. The signal is assumed to be a 50% modulation of uniform 1 mW/cm^2 illumination. The conductivity is 10^{-3} Ω^{-1}cm^{-1}, giving a maximum photoconductive gain of Γ_{max} = 9.6. For this example, the threshold for enhanced photoconductor performance is at 43 μm, and gain saturation occurs at widths below 13 μm.

Below a certain threshold of detector area, the photoconductor exhibits a superior SNR to the photodiode. This is a direct consequence of the internal gain mechanism of the

photoconductor: the noise is the same for both detectors, but the gain is for a photodiode is limited to one, whereas the gain for the photoconductor can be significantly greater than one.

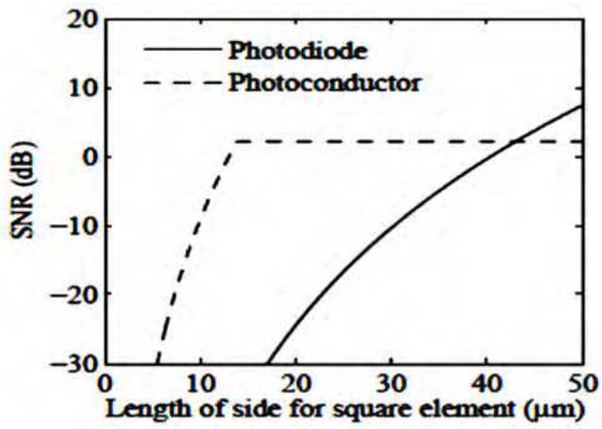

Fig. 1. Plot of SNR for a photoconductor and SNR of a photo-diode of the same square size as a function of the side-length.

2.3 Summary

In the limiting case of the thermal noise regime, where photon shot noise and current shot noise are dominated by the thermal noise of the load resistance, a detector with high internal gain is preferred. This thermal noise limit is approached at low light levels and at higher bandwidths, precisely the operating conditions required by speckle monitoring detectors for ultrasound vibration measurement. Both photoconductors and metal-semiconductor-metal detectors can exhibit internal gain at megahertz bandwidths with detector areas appropriate for direct speckle monitoring, and so merit further investigation.

3. Photoconductor development

This section describes the design and development process for the photoconductor prototypes built and tested at Dartmouth College for use in speckle monitoring applications. It also discusses several of the device characterization experiments performed on the resulting devices.

3.1 Gallium arsenide photoconductors

The first prototypes for speckle monitoring were constructed from GaAs (Heinz, 2004; Heinz, 2007; Heinz, 2003). They consisted of a raised mesa of GaAs 100 μm wide by several hundred μm long divided into four active areas defined and separated by superposed contacts. Each active area was approximately 100 μm $\times$ 40 μm.

Although quite sensitive to speckle motion, these devices suffered from a lack of bandwidth beyond some tens of kilohertz, and so were unsuitable for systems requiring ultrasonic bandwidths into the megahertz regime. It was determined that the limiting mechanism was most likely space-charge buildup, a result of high contrast in conductivity between the illuminated active regions and the shadowed contact regions.

Two potential solutions were investigated to reduce the effect of space-charge in the GaAs photoconductors and increase the individual detector bandwidth. The first of these

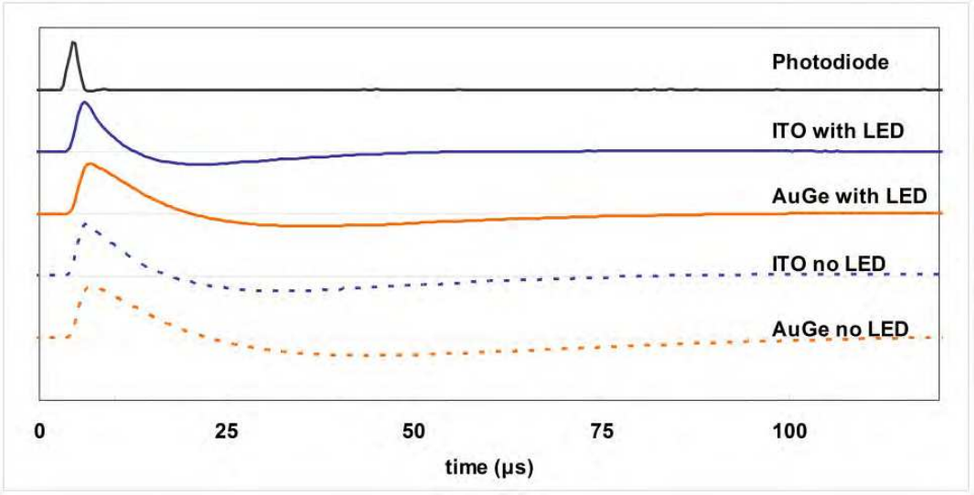

Fig. 2. Plot of GaAs photoconductor response to a 3 μs long laser diode pulse for various devices with and without LED background illumination. The response from a silicon photodiode is shown for comparison. The values on the y-axis are normalized (arbitrary units) (Bessette, 2006).

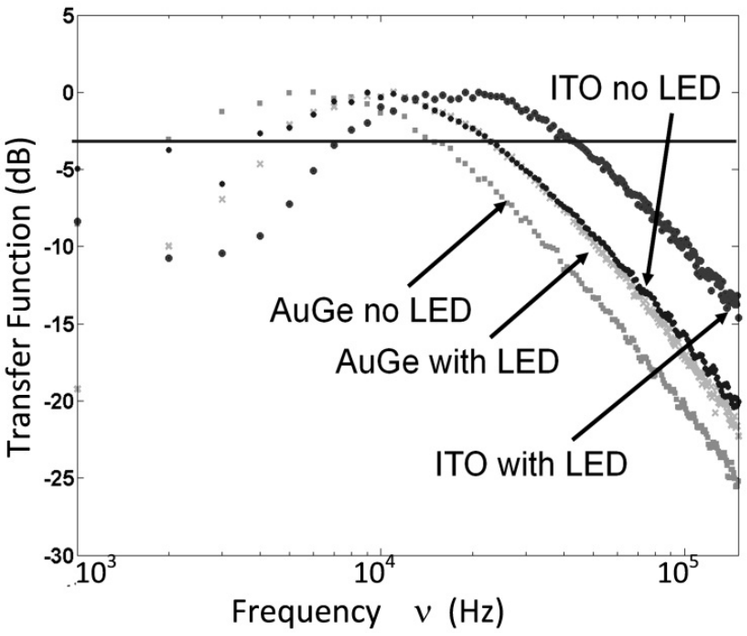

Fig. 3. Fast Fourier transform of AuGe and ITO device impulse response with and without red LED background illumination. The graph shows that the ITO devices are inherently faster than their AuGe counterparts with and without the 32 mW/cm² background illumination. The -3 dB rolloff for the un-illuminated AuGe device is around 10 kHz, while the ITO device rolls off at 20 kHz. With background illumination, the ITO device rolls off around 40 kHz (Bessette, 2006).

solutions was to use a transparent electrical contact, thereby lessening contact shadowing and reducing the impact of the resulting space-charge. To that end, a new GaAs prototype design was developed and produced (Bessette, 2006). The major improvement in this detector generation was the use of indium-tin oxide (ITO) for electrical contacts.

The second proposed solution for improving bandwidth was to provide a uniform background illumination with an LED during device operation. This would reduce space-charge buildup by shortening the space-charge relaxation time via increased average conductivity. Both of these measures were evaluated for effectiveness in a single impulse-response style experiment. Figure 2 shows the oscilloscope traces from different versions of the detector in response to an impulse-modulated laser diode. The settle time is seen to improve significantly with the presence of LED background illumination in both ITO and AuGe contacted devices. The settle time is also remarkably shorter for the ITO device, compared to the AuGe device. The photodiode response is limited by the diode laser driver which has a 200 kHz rolloff frequency. There was indeed an improvement in response time for the devices when using transparent contacts and background illumination, but as seen in Fig. 3, the gain in frequency response was still not enough to obtain ultrasonic bandwidth.

3.2 Silicon-on-insulators as a solution

To altogether eliminate the problems associated with persistent space-charge, a photoconductor array made from a relaxation-limited semiconductor was proposed. Silicon is a logical choice, since it is relaxation time-limited, responsive to visible and near-infrared wavelengths, and the most commonly used semiconductor material. The challenge with silicon is that in bulk form, the carrier diffusion length, or the distance on average that an unconstrained, excited electron or hole will diffuse before recombining, can be on the order of centimeters (Neamen, 2003). This rules out the kind of mesa architecture utilized in the GaAs array design, since the photo-generated carriers would escape from each element and diffuse throughout the crystal, destroying the spatial resolution required for speckle monitoring.

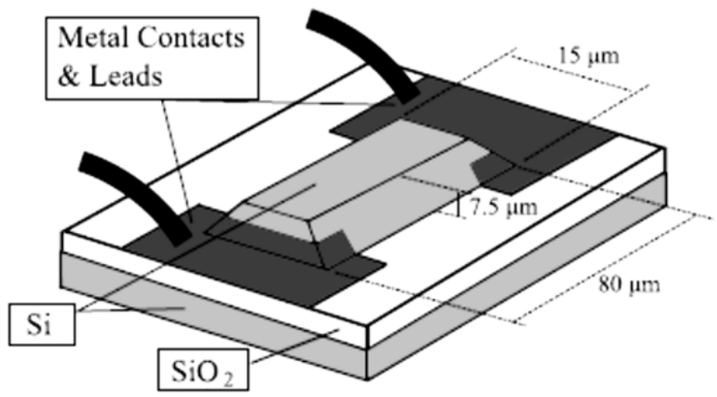

Fig. 4. Each detector element consists of an island of silicon bonded to an insulating layer of silicon dioxide grown on the silicon substrate. These structures are achieved by anisotropic etching through photolithographic masks. Electrical connection to each island is made by metal contacts, also defined by photolithography.

A new design was proposed incorporating silicon-on-insulator (SOI) technology, which consists of a thin layer of silicon crystal, on the order of 10 μm thick, fusion-bonded to a layer of insulating amorphous silicon dioxide grown on a supporting silicon wafer. Photoconductive islands are defined by etching through the thin top layer of silicon on every side, as is shown in Fig. 4. The mutual isolation of the islands in the array ensures that carrier diffusion will not compromise the spatial resolution of each detector element.

3.3 Fabrication details

The fabrication of SOI detector arrays, although they are comprised of only a few component layers, is not a trivial procedure to develop or execute. The difficulty arises as a consequence of both the small feature-size and the high aspect-ratio of individual photoconducting islands. The structures must be considered as fully three-dimensional, which makes processing in a top-down manner, the traditional approach to two-dimensional semiconductor wafer processing, more difficult.

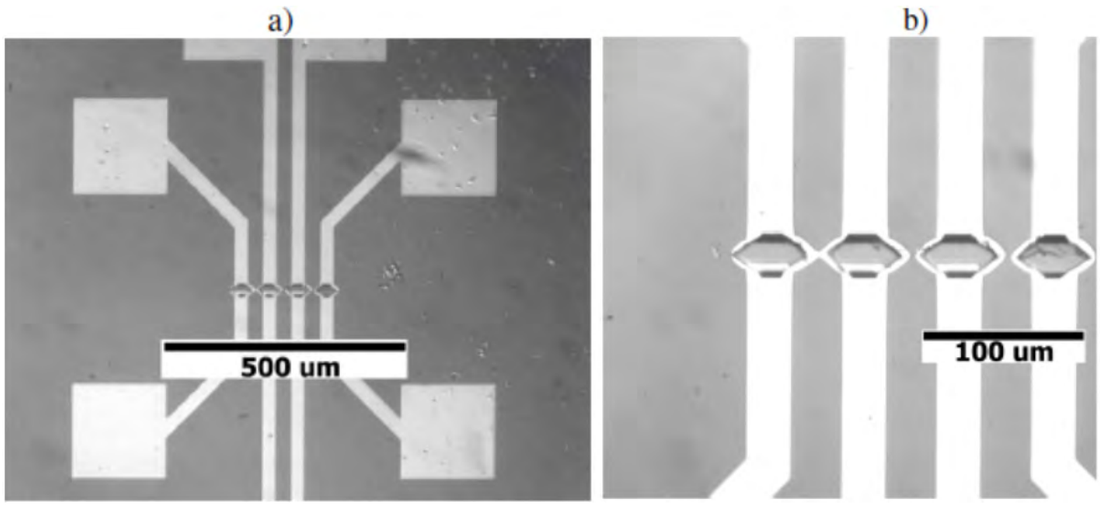

Fig. 5. a) Photograph of a finished four-element SOI photoconductor device array, including metal contact pads. In this design, each element can be contacted individually; b) Close-up of a finished four-element array. This sample was presumably underexposed during the contact layer photolithograpy step, resulting in a short circuit around the perimeter of each element after the metal etch step. This array was not actually used in experiments.

The following is an overview of the most current fabrication protocol for the SOI devices as designed for this project and executed in the available microfabrication facilities. An outline of microfabrication protocol:

1. RCA cleaning routine to remove surface impurities from wafer
2. Oxide layer grown on outer silicon layer
3. Photolithography step to define oxide etch
4. Oxide etch with HF, leaving oxide as a hard mask
5. Silicon etch with KOH
6. Metal contaminant removal and wafer cleanup
7. Optional removal of remaining oxide mask layer and optional oxide under-etch filling with hard-baked photoresist

8. Thermal deposition of chromium and gold layers to provide adhesive conducting layer
9. Photolithography step to define electrical contacts
10. Gold etch
11. Chrome etch
12. Mount wafer dice into electronic DIP package, connect leads to contacts

Optical micrographs of a finished sample that incorporates four individually addressable elements into a small array are shown in Fig. 5.

3.3.1 Anisotropic etching of silicon device layer

In order to facilitate the required electrical connections using top-down deposition of electrical contacts, a potassium hydroxide (KOH) anisotropic silicon etch step was chosen to define the mesa structures from the thin SOI device layer. KOH attacks the different crystal planes of silicon at different rates. Chiefly, there is a high degree of selectivity between the etch rate in the (100) direction of the crystal and the etch rate in the (111) direction. The (100) direction etches hundreds of times faster than the (111) direction. The result of etching with a mask edge aligned parallel with the <110> plane (that is, generally speaking, a mask edge aligned with the wafer flat of a (100) oriented wafer) is a sloped vertical etch exposing the <111> crystal plane, as is seen in Fig. 6(a).

This is in contrast to an isotropic chemical etch such as with nitric acid (HNO_3) based etchants, which would result an under-etched mesa, as in Fig 6(b). Under-etching is bad in this context for two reasons. Firstly, it would be very difficult to connect these devices electrically without removing the top oxide mask. Removing the oxide mask is undesirable since such a step would also partially etch the SOI buried oxide layer, further complicating electrical connection. Secondly, since the devices are almost as thick as they are wide, isotropic etching would eliminate the majority of the actual device. This problem only gets worse as the device dimensions are decreased. For these reasons the anisotropic etch was chosen.

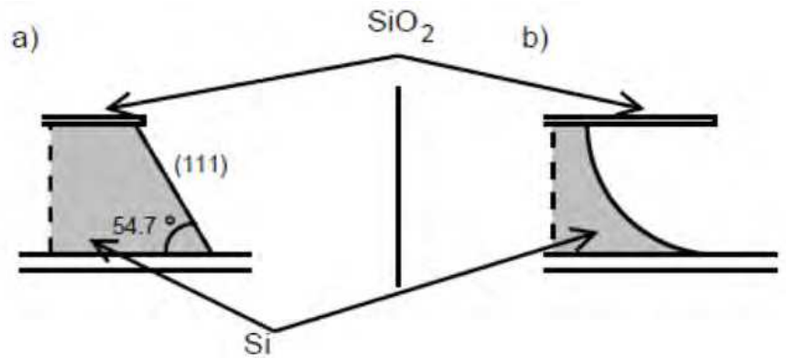

Fig. 6. Sketch of the side-view of silicon facets due to chemical etching a) Sloped vertical facet resulting from anistropic KOH etching of (100) oriented silicon. b) Under-etching resulting from an isotropic etch in which the device is etched laterally as much as it is etched vertically.

One difficulty encountered in utilizing such an anisotropic etch on these structures is the undesired etching of convex corners. There are many other crystal directions besides (110)

which etch faster than the (111) direction. When convex corners are exposed to the etchant, all of these other directions get etched, in addition to the desired downward etching (Lee, 1969; Wu, 1989). This results in convex corners that are etched inward, rapidly degenerating the structure from that direction. Fig. 7 shows the result of this effect, and demonstrates how this undesirable effect is exacerbated as device dimensions are reduced.

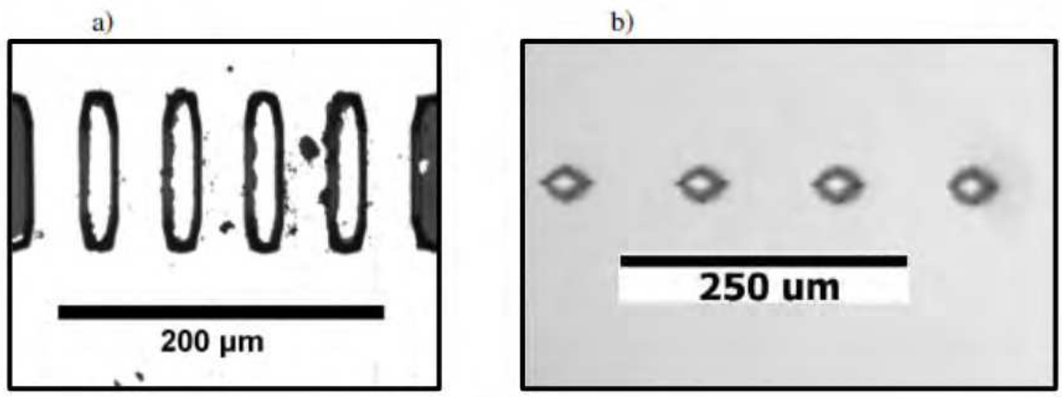

Fig. 7. The devices in prototype (a) are much longer than wide and the device layer thickness of silicon is only 7.5 μm, so the convex corner etching, while apparent, is not as significant. The devices in prototype (b) were meant to be more square, and the device layer thickness is 10 μm, which exaggerates the effect of the convex corner etching.

Convex corner etching is particularly problematic for these three dimensional structures, whose height is on the same order as their width. A common solution to this problem is to extend the etch mask over these corners (Wu, 1989; Biswas, 2006). The idea is to add extra sacrificial material that must be etched in the fast etching directions of the corner, thereby giving enough time for the vertical etch to finish before the protected corner material begins to etch. See Fig. 8 for a diagram of such a mask solution, after (Wu, 1989). Certainly, any new prototype including the anisotropic etch step during fabrication should include some form of convex corner protection in the mask design.

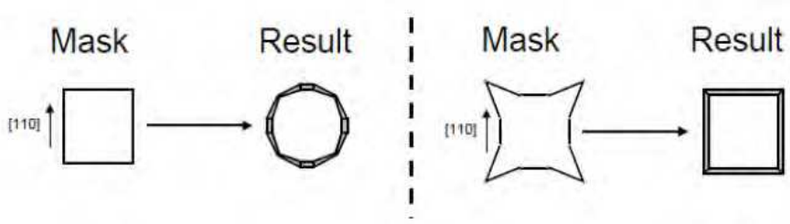

Fig. 8. Sketch of typical results of mask patterns for anisotropically etched structures with convex corners. The triangular overhangs on the mask help protect the desired corner integrity.

3.3.2 Electrical contacts

Early versions of the prototype used only a sputtered gold contact layer, but this was found to be insufficiently adhesive. In later prototypes, the contact layer was deposited via thermal deposition of a thin layer of chromium (to promote adhesion) of approximately 30 Å

thickness followed by thermal deposition of a conductive gold layer of approximately 2000 Å. These contacts proved to be robust enough to avoid excessive flaking, but they are not ohmic, as illustrated by the current versus applied voltage curve of a single device shown in Fig 9. The metal-semiconductor junctions formed by the contacts do exhibit rectifying behavior that typifies MSM photodiodes rather than a pure photoconductor. The next section discusses the implications of this result.

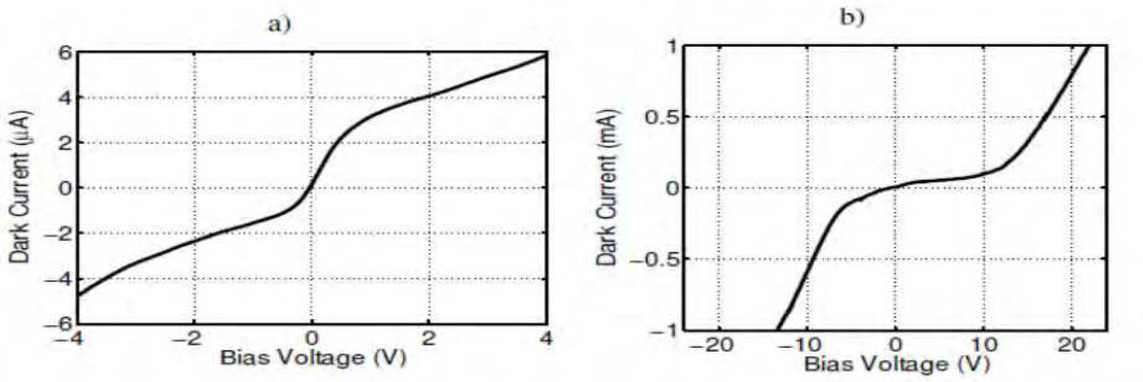

Fig. 9. Current versus bias voltage for an SOI detector with zero incident optical power a) near zero bias and b) extending into diode breakdown regions. The shape of the curve is typical of MSM photodiodes (Soares, 1992).

3.4 Characterization

After the prototypes were constructed, they were evaluated on different aspects of their performance, including the current-voltage relationship, gain, bandwidth, and noise.

3.4.1 Current versus voltage

Figure 9 shows the current versus voltage for one SOI device both near zero bias and over an extended range. The devices behave as metal-semiconductor-metal diodes already introduced in a previous section. Near zero bias (see Fig. 9(a)) there is a greater effective conductivity until one of the metal-semiconductor junctions is sufficiently reverse-biased to partially rectify the current, at which point the effective conductivity decreases. Note that the reverse bias current densities of these Schottky diodes are orders of magnitude greater than the equivalent *pn* junction diodes. Additionally, the barrier-lowering effects of the applied electric field result in a continuously rising reverse current. At even greater biases, the reverse bias current increases at a much faster rate due to ionization multiplication effects and eventually junction breakdown (Neamen, 2003; Tu, 1992).

Even without improving the contacts to be more ohmic, SOI MSM devices can still have the internal gain mechanism that makes them ideal for speckle monitoring applications with higher bandwidths. This has been discussed earlier and is illustrated in the next section on device characterization.

To optimize these devices for an extended range of ohmic behavior, some experimentation with the contact materials and deposition procedure will be required. Ohmic contacts in silicon devices are generally achieved by introduction of a heavily doped silicon region near

the contact, or by the use of silicide contacts (a silicon compound with a metal such as titanium, cobalt, tungsten, or platinum) rather than pure metals (Sze, 2007).

Additional doping would require at least one additional photolithographic and dopant implantation step, and is perhaps best to be avoided if possible. The formation of silicide contacts, however, requires only a slight modification of the contact deposition process and no additional photolithography. Silicide formation can be achieved in any one of four ways, including *direct reaction*, *chemical vapor deposition*, *co-evaporation*, or *co-sputtering* (Sze, 2007). Direct reaction is the easiest method to implement - it involves a metal deposition step followed by high temperature annealing. The metal component of the silicide is deposited (for instance by thermal evaporation or sputtering) onto the desired contact area. During the annealing step, some of the silicon device is consumed and becomes part of the contact silicide layer. A combination of careful literature review and experimentation should be sufficient to determine the appropriate metal choice and processing protocol for the formation of properly ohmic contacts with less rectifying effect on the current-voltage behavior of the photoconductors.

There is an apparent asymmetry in the biasing direction. This is possibly due to a difference in the metal-silicon junction size on either side of the element, which would make the reverse bias current in one direction greater than in the other. All elements in this array showed approximately the same shift with biasing applied in the same orientation.

3.4.2 Gain

The photo gain of an SOI device was measured as a function of bias voltage and compared to a silicon *pn* junction photodiode. The raw photocurrent measurements were converted to gain by calibration with a silicon photometer. In Fig. 10, we see that the silicon photodiode exhibits the expected flat gain throughout reverse bias. The gain value is approximately 0.85, indicating an internal quantum efficiency of about 85%.

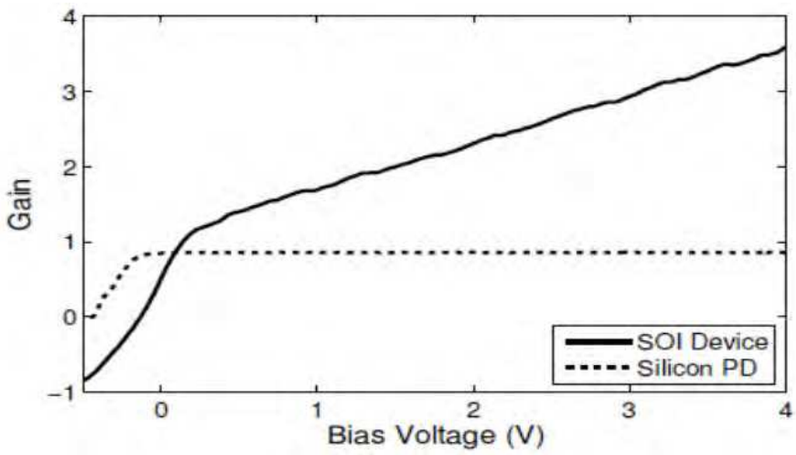

Fig. 10. Measured photo gain for an SOI photodetector (solid) compared to a reverse-biased silicon photodiode (dashed) as a function of bias voltage.

In contrast, the SOI device starts with a small gain near zero bias (due to the Schottky barrier induced fields). The gain increases sharply with applied voltage, quickly surpassing the *pn*

junction diode gain, until the bias reaches 0.20 V. At this point, the gain continues to rise linearly, but at a reduced rate.

Two related phenomena were discovered in the behavior of the photodetectors that were not initially predicted. Firstly, the gain increases monotonically with bias voltage up to a maximum and then declines again. It was thought that the gain would saturate, but not decline. Secondly, the gain is not independent of incident illumination, but actually decreases with increased light levels.

Figure 11 shows the block diagram of an experiment performed to demonstrate this behavior. A sweeping DC bias voltage was applied to one SOI element under illumination from two diode lasers. The first laser was a near-IR InGaAs diode that provided a constant background level of illumination. The second laser was an AlGaAs diode operating at 661 nm that provided a low level AC signal (10 kHz). The resulting photocurrent was filtered with a lock-in amplifier and recorded as a function of the bias voltage to obtain the curves shown in Fig. 12.

The peaking phenomenon at some bias voltage and the reduction in gain at high illumination levels can be understood in the context of carrier traps within the photoconductor crystal (Rose, 1958; Macdonald, 2001). The presence of traps in silicon and SOI that affect carrier lifetimes is well noted (MacDonald, 2001; Celler, 2003).

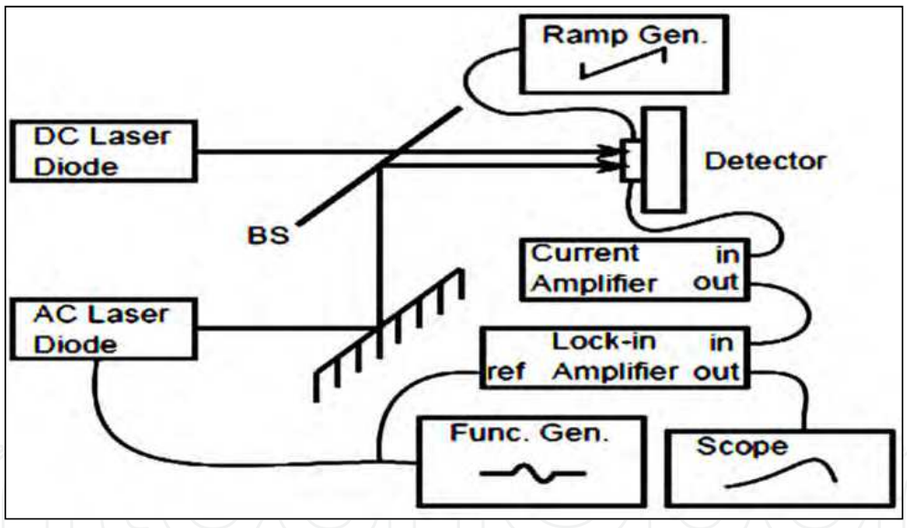

Fig. 11. Block diagram for experimental small-signal gain measurements as a function of bias voltage and background illumination.

Some trapping behavior can increase the effective lifetime of charge carriers; for instance, the presence of shallow traps in effective thermal equilibrium with the conduction band. These states capture some of the photogenerated carriers and prevent them from recombining and returning to the ground state. Since charges in these trapping states communicate with the conduction band, they can carry currents and contribute a photocurrent component with a long-lived response.

Another trap-related phenomenon that can contribute to the apparent long carrier-lifetimes is electron-hole separation due to the trapping of one of the charge carriers (MacDonald,

2001). For example, if holes are trapped in a state where electrons cannot recombine with them, a corresponding excess of free electrons will build up and contribute to the photoconductance (even if the holes do not contribute to the photoconductance).

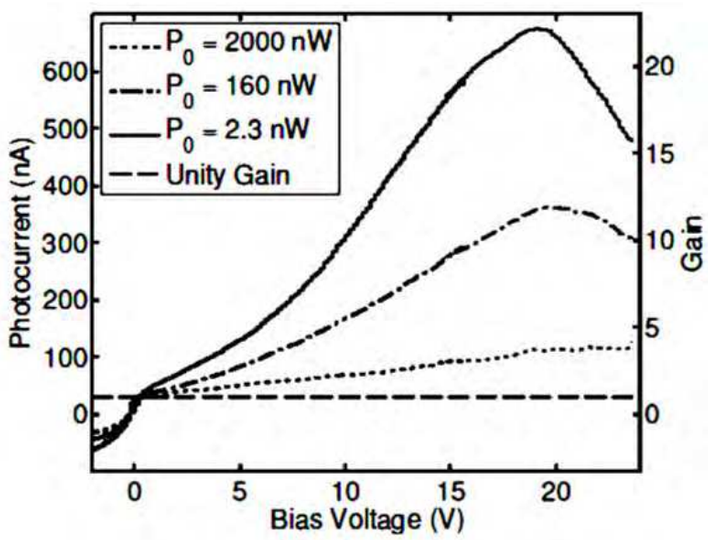

Fig. 12. SOI photodetector gain over a larger interval of bias voltage, for three levels of background illumination. The gain is a strong function of background illumination, presumably due to the sensitivity of the recombination time to trap-filling. Gain includes reflectivity losses.

The trapping states can become saturated by the two methods, as suggested by the curves in Fig. 12, both of which increase the density of excited charge carriers. The first is to raise the bias beyond the threshold to induce space-charge currents. The second is to expose the detectors to increasing levels of background illumination. In either case, the traps will begin to fill up and eventually become saturated.

At low carrier concentrations, these traps can significantly lengthen the effective carrier lifetime. Since the gain is proportional to lifetime (see Eq. 2), the gain is greatest when these traps are relatively empty and available to receive carriers. This phenomenon is also evident in the following impulse response and frequency measurements.

Since we know how much background optical power it takes to reduce the excess gain, we can make an estimate as to the density of these trapping states once we determine their effective lifetime. That will be determined in the next section.

3.4.3 Impulse response measurement

To determine if the prototypes were fast enough to operate at ultrasonic frequencies, an impulse-response measurement was made by exposing a device to a 10 ns square wave optical pulse from a 780 nm wavelength diode laser. Fig. 13 shows the recorded. response.

Beyond a certain bias level, the decay time of the response drops off dramatically, presumably due to the filling of shallow traps by excess dark current. Background illumination from a secondary laser diode also reduces the decay time of the detector response, presumably due to shallow trap filling.

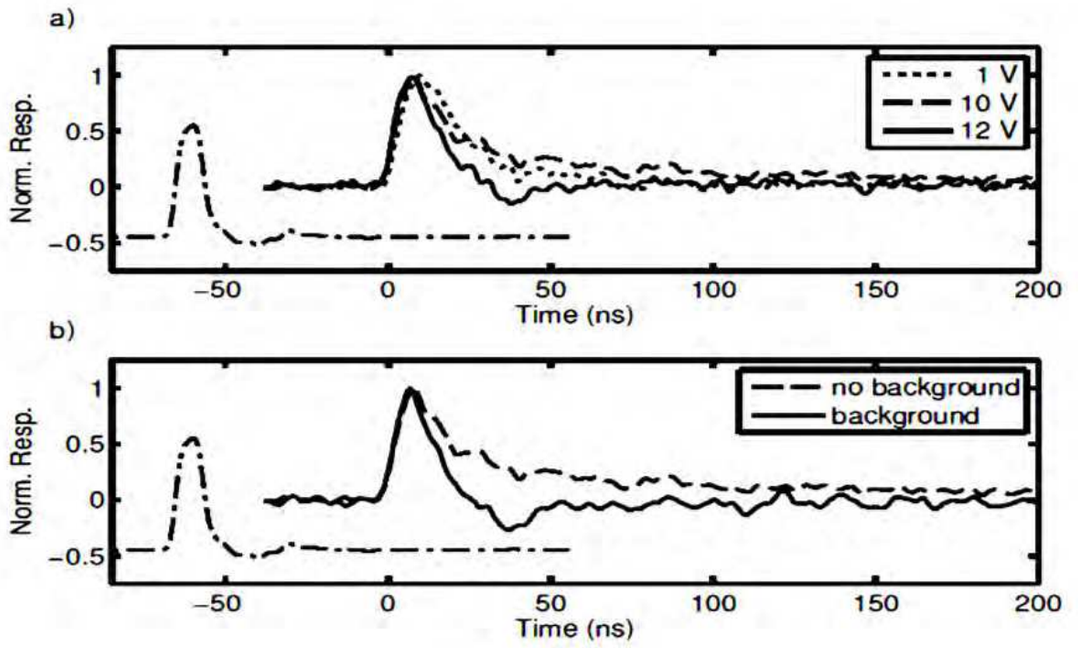

Fig. 13. Photodetector response to a 10 ns square pulse from a 780 nm diode laser under a) variable bias voltage with no background illumination and b) 10 V, bias with and without DC background illumination. Photodiode response for comparison is time-shifted to an earlier time for clarity.

Two things are immediately apparent. First, the bias voltage and background illumination greatly affect the decay time of the response. Second, even at its greatest, the detector response time is on the order of 50 ns. This indicates that the device should adequately measure signals well into the megahertz range with maximum internal gain, already measured greater than 20.

The impulse response appears to be composed of two components, a fast initial response and a slower decay. The slower component can be reduced by adding more bias voltage or by adding more background illumination. Fig. 14(a) shows the actual detector response, under minimal background illumination, modeled well by a double exponential decay with two time-constants, one at τ_1 = 6 ns and one at τ_2 = 90 ns. This secondary response, with the long decay rate, is responsible for the high gain at lower bandwidths up to a few MHz, as can be seen in Fig. 14(b). It is suppressed by either the excessive addition of bias voltage or by the application of strong background illumination, also illustrated in Fig. 14. Carrier lifetimes in this range, tens or hundreds of nanoseconds - much less than in bulk silicon - are often found in SOI structures (Mendicino, 1999; Rong, 2004). The lifetime shortening is due to the proximity of the active area to Si/SiO_2 interfaces.

We can make an order-of-magnitude estimate of the lower limit of trap carrier density by assuming that all of the high-intensity background light is absorbed by the long-lived trapping states, and furthermore that the states are evenly distributed throughout the device.

The power required to saturate those states multiplied by their effective recombination lifetime equals the total number of states in the device. We can see from Figs. 11 and 12 that

the traps seem to saturate when 1 μW or more is absorbed by the device. With a response time of 90 ns and a device volume on the order of 10^3 μm^3, this indicates that the trap density is at least 4×10^{12} cm^{-3}. Where they exist, these traps are probably considerably more dense, since a) the background light is not exclusively absorbed by the trapping states and b) the trapping states are most likely associated with the device interfaces and not distributed evenly through the device volume.

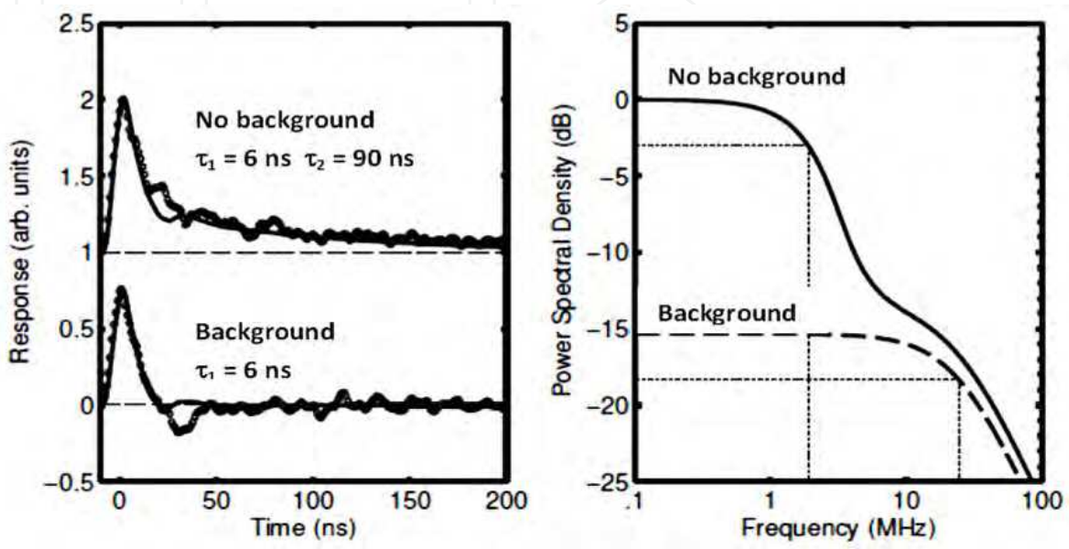

Fig. 14. a) Measured impulse response at 10 V bias (circles) overlaid with a fit of the double exponential impulse response (solid) for the detector with no background illumination and a single exponential response for the detector with significant background illumination. b) The frequency response of the fitted impulse responses. Note that detectors with sufficient (but not too much) bias voltage and low levels of background illumination show a significantly boosted response with bandwidths up to 2 MHz.

3.4.4 Detector noise

As already discussed, the best performance of the detector will be achieved when the SNR is maximized for a given level of illumination. This SNR value depends on both the noise levels and gain of the device. As long as the noise is dominated by the thermal noise term, which is unaffected by the bias voltage, the highest bias voltage (below saturation) and thus the highest possible gain should be used to maximize the SNR. Fig. 15(a) shows both the measured gain for the SOI device together with the combined thermal and current shot noise levels based on the dark current measurements. Assuming a 120 Ω load resistance and a 1 MHz detection bandwidth, the overall noise is dominated by the thermal noise component and is virtually unchanging until the bias voltage exceeds 10 V. All the while, the gain continues to rise with increasing bias, improving the signal-to-noise ratio.

However, as the bias voltage is increased, so is the dark current, which in turn increases the current shot noise. At some point, the dark current shot noise will become a significant portion of the overall noise. This increased noise will cancel the benefit of increased gain. The bias beyond which this happens can be determined by plotting both the gain and the noise on the same semilog plot, as in Fig. 15(b). When the slope of the noise versus voltage

exceeds the slope of the gain versus voltage on a logarithmic scale, the noise is increasing faster than the gain, and no benefit is obtained by turning up the bias more. The best SNR is obtained for this device somewhere around 15 V. The benefit of using detectors with enhanced internal gain in detector regimes dominated by thermal noise is nicely illustrated by this particular measurement. If the detector gain was limited to unity, about 1/20 of the actual measured value, the best the detector could achieve in terms of SNR is less than 0.2% of the actual measured value. This is obviously a significant improvement.

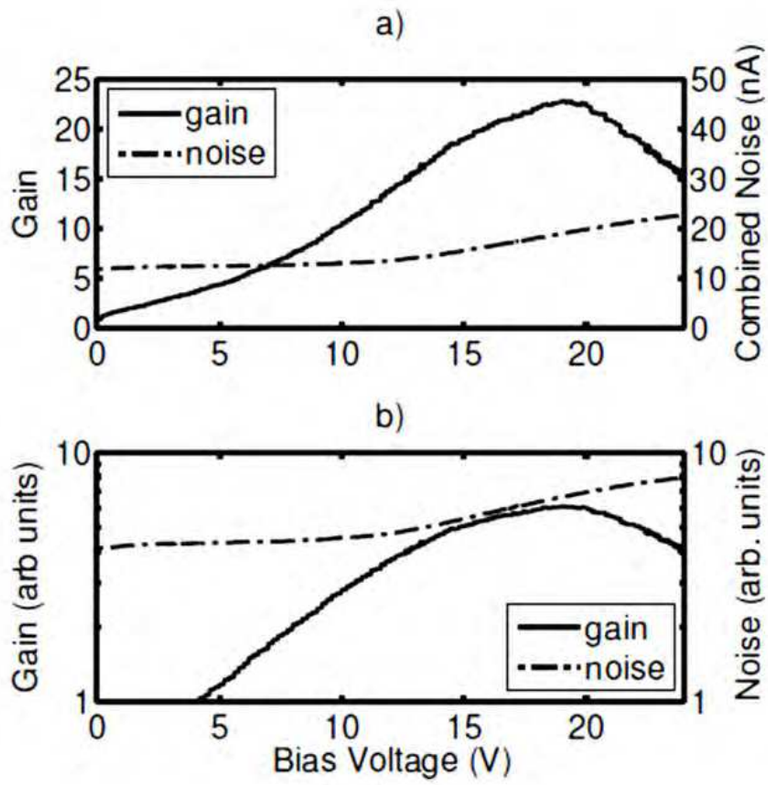

Fig. 15. a) Internal gain and detector noise as a function of bias voltage; b) The same values plotted on a semilog scale. When the slope of the noise exceeds the slope of the gain, the noise increases faster than the gain, and there is no benefit from increasing the bias. Combined detector noise is calculated assuming thermal noise of a 120 Ω load resistance and the shot noise associated with the measured dark current values. A detection bandwidth of 1 MHz is assumed.

3.5 Summary

Gallium aresenide photoconductors of the type discussed in (Heinz, 2004, 2005, 2007, 2008) were determined to be too slow for megahertz detection of speckle motion due to the buildup of space charge, even with the slight improvement of transparent electrical contacts and background illumination. Silicon mesa structures were developed that do not suffer from the same space-charge bandwidth limitations. The mesa architecture provides spatial isolation of each detector, and the prototypes proved to be fast enough to operate at megahertz frequency.

The current-versus-voltage curves for the prototypes show behavior that is more like MSM photodiodes than a true photoconductor, but this is acceptable since MSM devices can have greater than unity gain, which is the important characteristic for high-speed speckle-monitoring. Indeed, the internal gain was measured as a function of bias voltage and found to have a maximum for one device at about 23. The gain is greatest for biases below 20 V and at low levels of illumination due to the trap filling effects of large dark currents and photo-generated charges.

It was also shown that when operating at MHz bandwidths, the noise is indeed dominated by the thermal noise component of the load resistance even at relatively high bias voltages. The SOI device was determined to have a maximum SNR roughly 500 times greater than an equivalently sized silicon *pn* junction diode operating under the same conditions.

4. Optical generation and detection of acoustic waves with an experimental direct speckle monitoring system

This section discusses experimental demonstrations of speckle monitoring-based vibration measurement using the photo-conductor mesa detectors coupled with optical techniques for acoustic excitation. There are many reasons to develop a system that exploits the optical excitation of acoustic waveforms as well as their optical detection. Fully non-contact systems can be less invasive, less disruptive to the device under test, and in some cases more rapidly deployed. Extensive work on the subject is available in the literature (Scruby, 1990; Davies, 1993; Pierce, 1998) that will only be summarized briefly here. Some understanding of the different mechanisms involved will help us better understand the experimental results obtained from tests with the photo-conductive mesa detectors.

4.1 Optical generation of acoustic waves

Generation of ultrasound waves with laser beams in untreated surfaces can be divided into two categories (Davies, 1993):

i. The thermoelastic regime describes acoustic waveforms generated by expansion and compression resulting from the localized heating caused by an optical pulse. Typical peak optical intensities supplied to the surface in this regime are $< 10^7$ W cm^{-2} (Scruby, 1990).

In the thermoelastic regime, the acoustic source (the bit of solid material that actually moves in direct response to heating, setting the acoustic wave in motion) is roughly a disc with a diameter equal to the width of the impinging laser beam and a depth determined by the thermal conductivity of the material and the rise-time of the laser pulse (Scruby, 1990; Davies, 1993; Pierce, 1998). For metal samples, and for nanosecond pulses (from a Q-switched Nd:YAG pulse, for instance), the source depth is on the order of microns, but can grow to hundreds of microns for millisecond rise times (Scruby, 1990; Pierce, 1998). As a result of heating, the disc exhibits expansion, predominantly in the plane of the surface (Pierce, 1998).

ii. The ablation regime pertains to acoustic waveforms generated by the momentum transfer of evaporated material ejected from a rapidly, locally heated component of the test object's surface. Typical peak optical intensities supplied to the surface in this regime are $> 10^7$ W cm^{-2} (Scruby, 1990).

In the ablation regime, the acoustic source is a cloud of vaporized material forming a plasma just above the surface and moving rapidly away from it. The result is an acoustic impulse directed predominantly normal to the surface.

In addition to peak powers and the *temporal* profile of the laser beam, the *spatial* profile of the laser beam as it intersects the solid surface is crucial in determining the final acoustic waveform injected on the test object (Monchalin, 2007; Khang, 2006]. The beam shape can be tweaked to encourage or discourage coupling into one or more acoustic modes. For instance, an optical grating can be imposed on the object surface with a spacing corresponding to the wavelength of the desired surface acoustic wave. This can greatly enhance coupling into that mode. Since no effort was made to explore this aspect of optical ultrasonic generation during the course of this project, no further discussion will be given to this topic. However, this remains a rich area for study, in particular learning how to promote the in-plane acoustic modes – we have already seen how photoconductive mesas are well suited to the detection of such waves, through speckle monitoring.

4.2 Nd:YAG pulsed laser generation of ultrasound waves

An experiment was performed in which ultrasonic waveforms were produced in solid metal targets by surface-ablation with a Q-switched Nd:YAG laser pulse. The various samples under test were thin strips made from unpolished aluminum, copper, and stainless steel. The resulting acoustic waves were allowed to propagate through the strips and were detected by a speckle monitoring system that observed a point on the test object located some distance away from the acoustic source.

The interest in these experiments is two-fold. Firstly, they show how well the photoconductive mesas monitor direct speckle motion, providing a sensitive method for remote ultrasound detection, especially for detection of in-plane surface motion to which other detection schemes are not as selectively sensitive (Monchalin, 1986). Secondly, they provide a demonstration of the bandwidth capabilities of the SOI photoconductive detector mesa prototypes made in our laboratories.

4.2.1 A_0 antisymmetric mode Lamb waves

Acoustic waves that propagate in the plane of thin plates and membranes can be decomposed into different Lamb wave modes. The two main classes of Lamb wave are the antisymmetric modes, for which the front and back surfaces of the plate move out of phase with respect to the middle of the plate and the symmetric modes, for which the front and back surfaces move in phase. For low frequencies, below some cut-off value that depends on surface thickness and plate material, we saw that only the lowest order modes, A_0 and S_0 exist. Which of these gets excited depends on the type and geometry of the exciting pulse.

Fig 16 shows the experimental arrangement for the first test, in which the Nd:YAG laser is directed onto the back planar surface of the strip. This directs most energy into a direction perpendicular to the surface (flexing), which is the primary motion of the A_0 mode. The antisymmetric mode should be the dominant acoustic waveform resulting from this excitation (Pierce, 1998). The detector output confirms this hypothesis, as there is clear evidence of antisymmetric Lamb wave propagation in the strips, and very little evidence of symmetric Lamb waves. In Fig. 17, we see a comparison of the recorded signal and the theoretical calculations of the A_0 mode propagating through the same distance of an

aluminum sheet. The calculations assume a square impulse excitation of the A_0 mode with the bandwidth of the recorded signal. The dispersion relation is $V_p = 2V_S(1 - V_S^2/V_L^2)\beta b/(2\bullet 3^{1/2})$, where V_p is the phase velocity of the mode, V_S is the shear velocity of the material, V_L is the longitudinal velocity of the material, β is the wavenumber of the mode, and b is the plate thickness, according to Chapter 9 of (Cheeke, 2002).

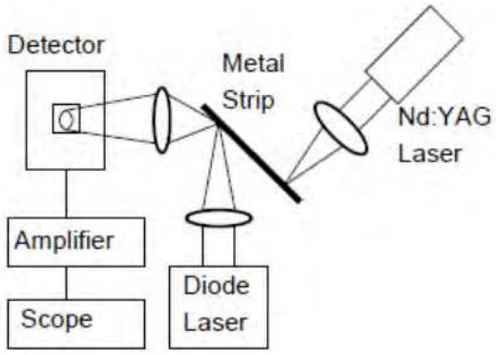

Fig. 16. Experimental arrangement for pulsed Nd:YAG laser excitation of ultrasound in metal strips. Detection of ultrasound was made with a speckle monitoring photoconductor.

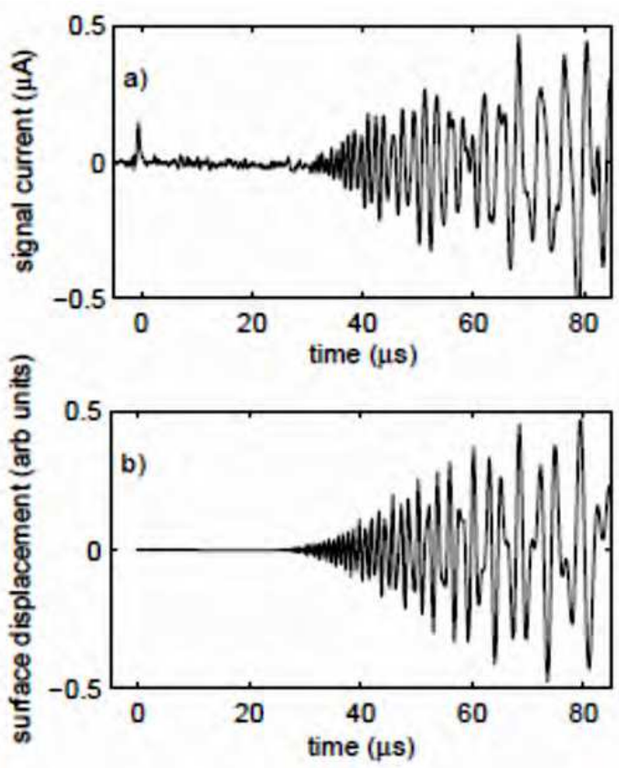

Fig. 17. a) Oscilloscope trace of an acoustic vibration generated with 7 cm of separation between the Nd:YAG pulse and the reference spot. The initial spike in photocurrent comes from the Nd:YAG pulse at time $t = 0$. b) Calculated surface displacement caused by A_0 Lamb waves propagating a distance of 7 cm. One reflection from the far edge of the strip (1 cm further from the detection point) is included to illustrate the effect of interference.

Figure 18a depicts the signal obtained from the copper strip, showing the arrival of multiple distinct waves. By looking the spectrogram in Fig. 18b, it is clear that each of these waves shares the same dispersion relation. Thus each wave is an instance of the same acoustic mode (A_0). These secondary instances are most likely reflections from one of the copper strip edges.

The antisymmetric mode is certainly useful, especially for extracting material properties from samples. For just one example, there is great interest in online monitoring of paper stiffness, consistency, and quality with laser ultrasonics exploiting antisymmetric Lamb waves (Brodeur, 1997). The thickness and shape of thin film structures, especially during fabrication (Pei, 1995), is another parameter of interest to which the propagation of such Lamb waves are sensitive. Any all-optical method for such measurements is certainly worth a consideration.

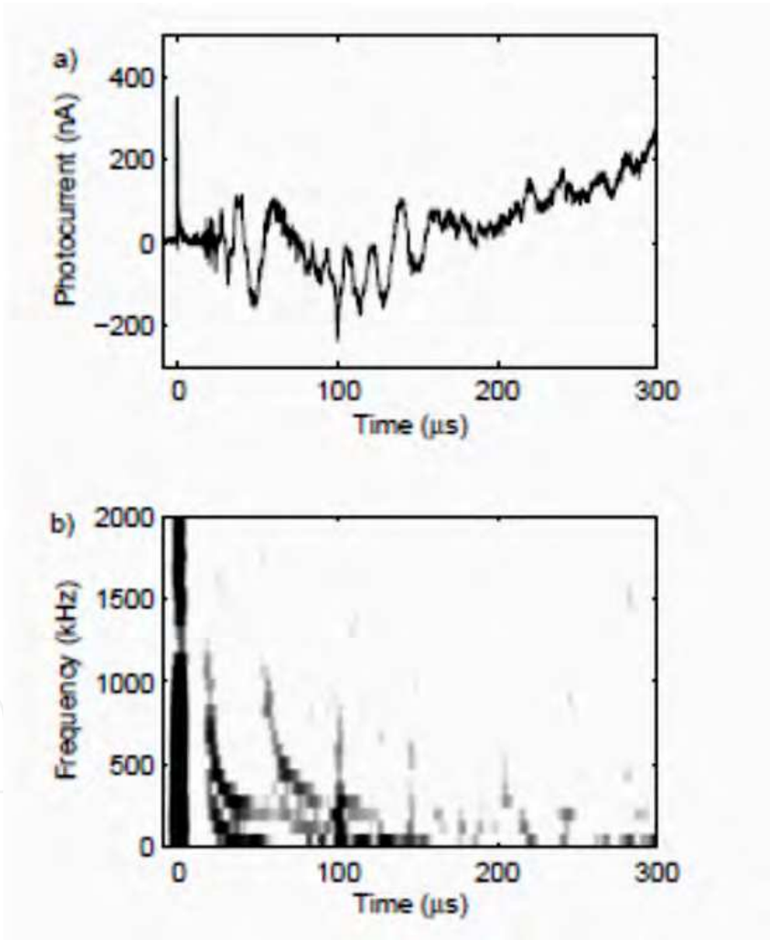

Fig. 18. (a) Oscilloscope trace of ultrasonic waves traveling in a copper strip with (b) corresponding spectrogram showing the spectral content of distinct waves as a function of time. The initial spike at time t = 0 comes from stray Nd:YAG light and serves as a marker for the onset of sonic excitation. At least the first two modes appear to have the same dispersion relation, indicating that they represent the reflection of a wave in the same mode (A_0).

4.2.2 S_0 symmetric mode Lamb waves

The lowest order symmetric mode (S_0) is of particular interest to applications that record the timing of pulse echoes. This would include parts inspections for internal cracks and discontinuities (Lowe, 2002). The reason for this is that the S_0 mode suffers very little dispersion, limiting pulse breakup and allowing for better event timing. Furthermore, at low frequencies, the S_0 mode is dominated by in-plane surface motion (Cheeke, 2002), so that is it is particularly well-suited to observation by a speckle monitoring system.

One problem with using the S_0 mode is that it is more difficult to excite by Nd:YAG laser pulse than the A_0 mode. Striking the flat surface of a plate tends to put most acoustic energy into the A_0 mode. The dominant motion of the S_0 mode is compression in the plane of the plate, so it is easier to excite this mode by striking the thin plate edge, as in the arrangement of Fig. 19. Although edge-excitation has been investigated with traditional contact transducers (Lowe, 2002), this novel arrangement is the first all-optical, end-on excitation technique specifically designed to excite only the symmetric mode. With further improvements, it could be adapted to generate in-plane vibrations for testing in any kind of plate-like structure.

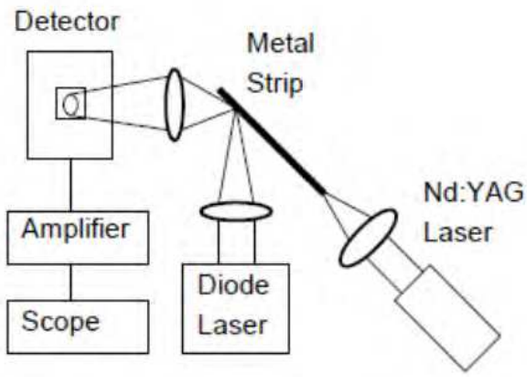

Fig. 19. Edge excitation of metal strip with Nd:YAG laser pulse.

When edge excitation is used, the coupling efficiency into the S_0 mode is dramatically enhanced, as can be seen in the oscilloscope trace in Fig. 20, showing the resulting vibration of such excitation in a stainless steel strip. This arrangement provides better timing information due to the non-dispersive nature of the S_0 waveforms. The waveform in this case is more or less a single pulse, about 10 μs wide, with a slightly exaggerated tail.

The round-trip travel of the wave is clearly discernible from the detector output in the first 300 μs of the recorded signal. The wave first arrives (after traveling just under one length of the strip) after 18 μs, and subsequently every 37 μs or so after that.

Although the Nd:YAG pulses produce ultrasonic pulses in these strips that can be used to investigate the material and geometric properties (for example, sheet thickness and points of internal reflection), this method can hardly be called "nondestructive." The material ablation that causes the acoustic impulse leaves a crater in the object surface. Repeated impulses, especially on delicate structures and thin films, require a gentler approach.

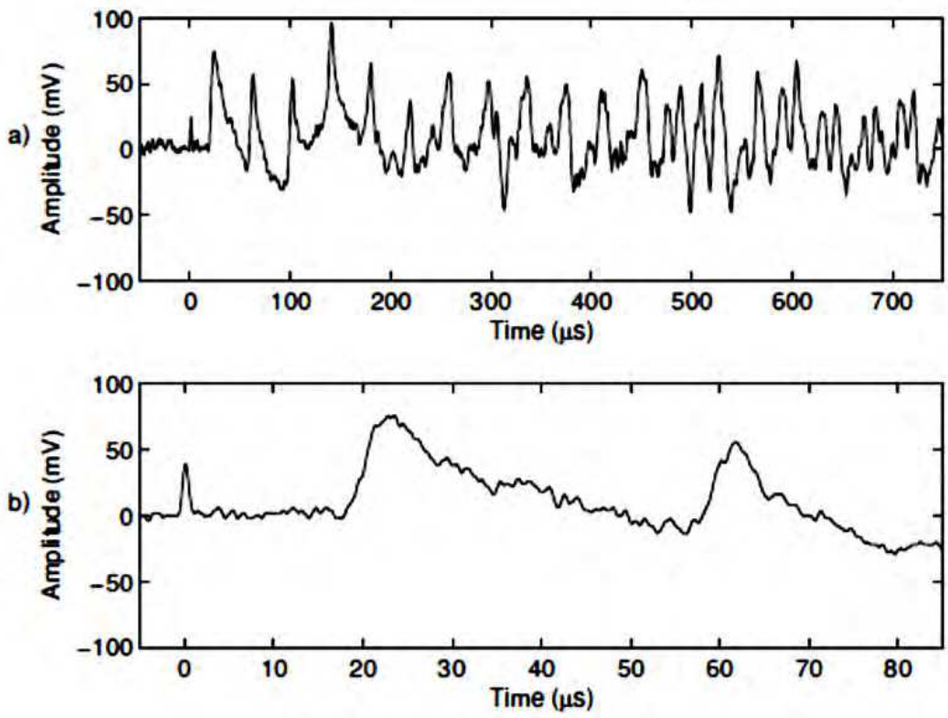

Fig. 20. Vibration signals recovered during edge excitation experiment. The spike at time t = 0 is from scattered Nd:YAG laser light, marking the onset of acoustic excitation. This S_0 waveform is much less dispersive than the A_0 mode, allowing for more precise timing of discrete events, such as reflections. a) For the first 300 μs or so, the waveform is dominated by repeated reflections of the non-dispersive acoustic wave from either end of the strip as it traverses the detection point. b) At a smaller time scale, the time separations between peaks are easier to see. The time (37 μs) between the first pass of the wave and the second pass, or one round trip of the wave, is just slightly more than twice the delay (18 μs) between excitation onset at the far end of the strip and the leading edge of the first pass. This is precisely what is expected from the experimental geometry, depicted in Fig. 19. The mode velocity as measured by the temporal separation of the peaks is 5200 m/s.

4.3 Laser diode generation of ultrasound

To produce ultrasound in a truly nondestructive manner, one must restrict oneself to the thermoelastic regime of optical ultrasound generation. This can be achieved by lowering the peak power below the damage threshold. That approach favors the use of technical finesse over raw power, for which laser diodes are a good alternative to the Q-switched Nd:YAG laser. Consider the experiment in Fig 21, in which the Nd:YAG excitation laser has been replaced by an InGaAs current-modulated diode laser with a peak output power of approximately 50 mW in a surface-normal configuration. Figure 22 shows the detector output for an aluminum foil strip with dimensions 10 cm × 0.5 cm in response to excitation pulses of various widths. A 1 ms excitation pulse produces a large vibration that is easily measured by the speckle-monitoring detector. Even with such low coupling-efficiency, there is some diagnostic capability with this simple configuration, for instance monitoring low-frequency standing waves in small structures.

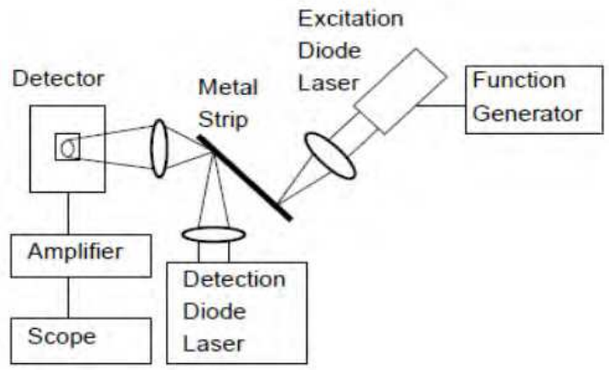

Fig. 21. Experimental setup for measuring the impulse response excited with a current-modulated laser diode. For the data presented in Figures 22 and 23, the metal targets were strips of aluminum foil.

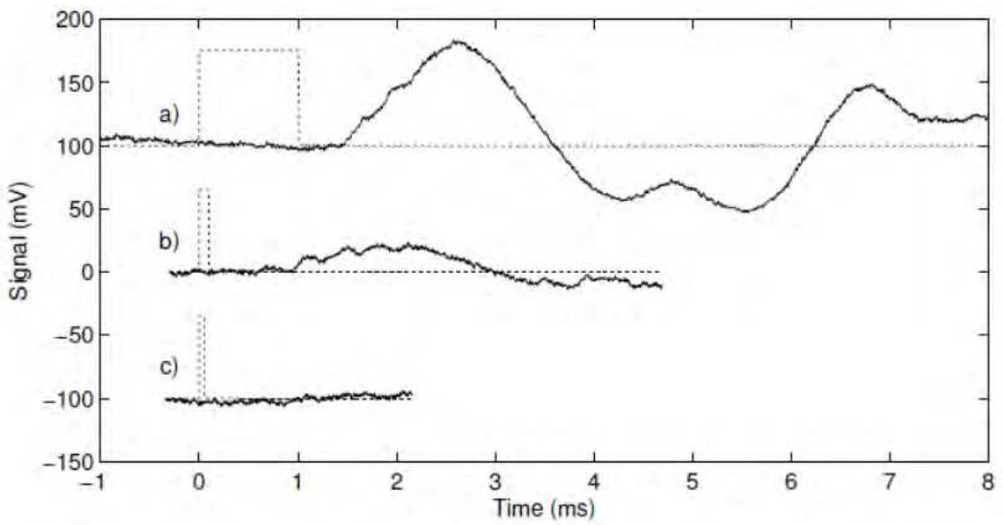

Fig. 22. Waveforms in an aluminum foil strip resulting from thermoelastic generation with an InGaAs laser diode pulse with a peak power of 50 mW and spot size of approximately 1 mm. Dotted lines indicate the period of laser diode excitation, solid lines indicate the detector signal. Three pulse lengths are shown: a) 1000 μs, b) 100 μs, and c) 50 μs. Decreasing the overall optical power delivered to the metal shows a corresponding decrease in the amplitude of the detected signal. For pulse widths less than 50 μs, the signal is no longer discernible from the noise.

Consider the data shown in Fig. 23. Three aluminum foil strips, 10 cm × 0.5 cm, were gently stretched flat and anchored on either end with approximately equal tension. Two of the three strips were left unaltered, but in the third strip a small tear was introduced into the strip's edge halfway between the excitation and detection points. Each strip was excited by a 500 μs square wave impulse from the excitation laser diode. The impulse responses of the two undamaged strips look nearly identical, a fundamental vibration with a period of about 4.7 ms ringing down at approximately the same rate. The damaged strip does not ring as cleanly. Although the fundamental frequency looks approximately the same as for the

undamaged strip, the signal is disrupted by some other vibrations. Without analyzing the precise differences in the impulse response signature between the healthy and the damaged strips, it is fair enough to say that there is a clearly discernible difference. Such a distinction could be used to detect the presence of damage.

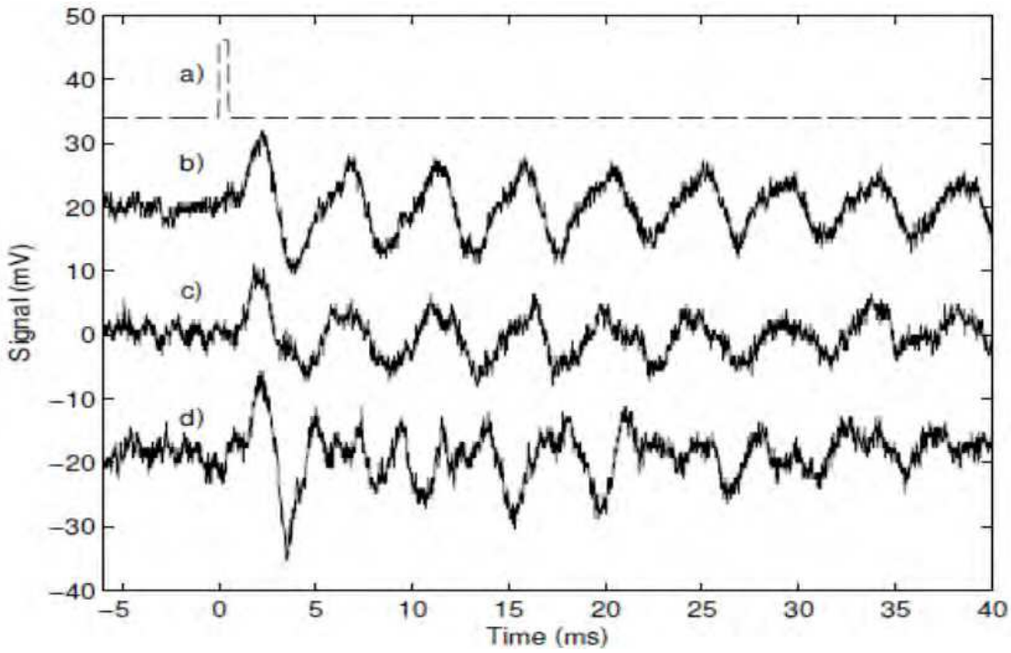

Fig. 23. Response of three identically sized aluminum foil strips under equal tension to a 500 μs rectangular pulse from a diode laser. a) Excitation diode current (arbitrary vertical scale), b) strip 1, no defect, c) strip 2, no defect, and c) strip 3, a tear introduced between points of acoustic generation and detection.

Although useful, this low-frequency, resonance technique is not perfect for every solution. Some applications are best served by a different approach to acoustic imaging that requires temporally and spectrally resolved pulse information such as time-of-flight and dispersion data. This generally precipitates the use of higher-bandwidth acoustic regimes.

The obvious drawback to operating in the thermoelastic regime is the decrease in acoustic power delivered to the object of interest. This problem can be addressed by using selective filtration methods on the detector signal, such as lock-in amplification and input-output signal correlation techniques.

4.4 Summary

In this section it was shown that speckle-monitoring is a viable technique for the remote detection of acoustic waves, in particular ultrasonic waveforms that are useful for material characterization and structural examination. The possibility of coupling speckle-monitoring with optical ultrasound generation is particularly attractive, as it allows for a completely non-contact system. Speckle-monitoring is especially appealing for use in measuring in-plane ultrasonic waves, such as the S_0 Lamb wave mode measured in the edge-excitation experiment, since it is selectively sensitive to that type of motion, unlike most other optical

vibration detection schemes. There is an incentive to restrict optical excitation to the lower-power thermoelastic regime, such as by using current modulated CW laser diodes.

5. SOI speckle monitoring: detection limits compared to alternatives

Having laid the framework for characterizing the SOI detector prototype and conducting preliminary experiments, we are in a position to make some statements about the viability of this technique as an alternative to other optical vibration measurements. This section quantifies those comparisons and indicates certain applications to which speckle monitoring with photoconductor arrays is best suited. Numerical values are reported as rough estimates constructed from the data gathered in the previous chapters.

5.1 Pure in-plane-motion

After establishing that measurement with such a system is indeed possible, the most obvious question to ask about a particular measurement scheme for a given application is "how sensitive is it?" To that end, this section will attempt to answer that question for the direct speckle-monitoring method and other comparable techniques under similar circumstances.

Since we have already established that speckle-monitoring is most effective for in-plane measurement, we will focus on that application. As a convenient metric for the lower limits of sensitivity, let us define the quantity δ_{min} to be the minimum detectable displacement that produces a signal with amplitude equal to the noise for a given system output. Since we have seen that sensitivity generally scales in proportion to optical power and inversely to bandwidth, δ_{min} will be given units of m $Hz^{-1/2}$ W, where the power is the total available laser power.

5.2 SOI Detectors, single element detection limit

The minimum detectable photocurrent is equal to the noise current, which from experiments is roughly 20 nA at 1 MHz bandwidth with an overall gain of 20 across a load resistor RL = 50Ω. Since noise scales with the square root of the bandwidth, we can estimate a noise figure of σ_n = 20 pA•$Hz^{1/2}$. A gain of 20 corresponds to a responsivity of about $\Re$ = 10 A/W at 633 nm. This means that the minimum detectable change in collected power per element is P_{min} = 2 pW•$Hz^{1/2}$.

The amount of speckle translation required to achieve this change in photocurrent depends on the optical system and how much optical power is collected. For a small scattering spot whose width is S, illuminated with a total power P_S, the speckle size in the detector plane is approximately $\varepsilon = \lambda B/S$, where B is the optical matrix element. Assuming the light is scattered equally in all directions and the scattering spot size $S << B$, the average speckle intensity is approximately $I_0 = P_S\lambda^2/(2\pi\varepsilon^2S^2)$ as shown in (Dainty, 1975, Bessette, 2010). For a small translation δ_s of the speckle pattern, this means the detector will see on average (considering the ensemble of all possible random speckle patterns) a change in collected power given by $\Delta P = I_o\,\varepsilon^2\,(\delta_S/\varepsilon) = P_S\lambda^2\delta_S/(2\pi\varepsilon S^2)$, where we have assumed that the speckle width is matched to the detector width. Setting ΔP = to ΔP_{min} and solving for δ_s, we find that the minimum measurable motion is

$$\delta_{S,min} = 2\pi\varepsilon S^2 \Delta P_{min}/\lambda^2 P_S \quad .$$

Using a typical scattering spot size of 0.5 mm and a detector-matched speckle size of 20 μm, this gives $\delta_{S,min}$ = 160 pm Hz$^{1/2}$ W. This is the minimum detectable translation of the speckle pattern. Typically, there will be optical magnification in this system with a value ~10, so this yields a minimum detectable displacement on the order of δ_{min} = 16 pm Hz$^{1/2}$ W.

For example, with a 1 W laser source and a bandwidth of 1 MHz and using a 50Ω load resistor, the detection limit is approximately δ_{min} = 16 nm for a single element. This value can be brought down even more by using a larger load resistor, as large as the bandwidth limitations will allow.

5.3 Other methods

Classical interferometry can be used to detect in-plane motion under certain conditions. For instance, rather than using one beam to illuminate the object and one reference beam, the differential interferometry approach uses two beams to illuminate the object (Monchalin, 1986). If the input aperture of the system and the illuminating spot are sufficiently small, then what forms in the detector plane is essentially a single speckle. The phase of that one speckle is sensitive to motion parallel to the difference in wave-vectors of the two illuminating beams. If the two beams illuminate the surface at equal but opposite angles with respect to the normal, the setup is sensitive purely to motion in the plane of the object. Using a 0.5 mm spot size and a HeNe laser with a wavelength of 633 nm gives a detection limit δ_{min} = 16 pm Hz$^{-1/2}$ W. With a 1 W laser and 1 MHz bandwidth, a sensor with these parameters has a detection limit on the order of δ_{min} = 16 nm. Again, this can be reduced by increasing the load resistor to the maximum the bandwidth requirements will allow. We see that the detection limit for the direct speckle monitoring method with SOI detectors is roughly equal to the interferometric method. The speckle monitoring method has the greatly added advantage that it does not require two coherent beams to be precisely overlapped at a specific angle in a small spot.

Speckle photography relies on tracking individual speckle features as they move across the detection plane with an electronic detector array. These methods are generally used in low speed applications -- CCD arrays with low read-out rates and long integration times (on the order of milliseconds). A recent report on different algorithms (Cofaru, 2010) finds that resolution is on the order of 10^{-3} pixel widths, generally speaking around δ_{min} = 10 nm. Although this is on the same order as the detection limit of the SOI sensor, the SOI photoconductive mesa sensor described here does so at 1 MHz bandwidth.

Spatial filtering of moving speckles is a subcategory of speckle photography in which image processing of the speckle pattern is done in real-time by spatially filtering the speckle pattern with a periodic mask (for example a simple Ronchi grating) and integrating the filtered light (Komastu, 1976). As the speckle pattern translates across the grating, the integrated signal is periodic with a period equal to the time it takes an individual speckle to translate a distance equal to the grating spacing. The frequency of the integrated signal is proportional to velocity, so this technique is generally used to measure surface velocity. The measurement depends on determining a temporal frequency, so there must be at least one full period observed. This means that the speckle must travel at least the distance of a grating spacing. Since signal-to-noise is best when the speckle is about the same width as the

grating spacing (Kamshilin, 2009), the detection limit is approximately 10 μm. This method is not nearly as sensitive to small displacements as the other methods discussed; however it works well for high in-plane velocities when the object is moving a large distance.

5.4 Summary

We have shown that photoconductive mesas directly monitoring speckle motion have an important place among applications requiring higher bandwidth detection of in-plane motion. The detection limit for a single element monitoring in-plane motion is on the order of δ_{min} = 16 pm $Hz^{-1/2}$ W.

6. Arrays of photoconductive mesas

The performance of speckle monitoring systems can be dramatically increased by using multiple detectors to make simultaneous measurements of a single speckle pattern displacement. An array configuration of photodetectors can be used to enhance the signal to noise ratio of displacement measurements. In addition to a lower noise floor, uncertainty in absolute displacement measurements can be mitigated. Additionally, the adverse effects owing to harmonic distortion can be lessened by the use of arrays, all allowing for better overall system calibration.

The signals from multiple array elements can be combined in a way that reduces noise in the same spirit as simple averaging. The contribution of each element to the average, however, must be weighted according to the particular speckle that element is monitoring. The primary challenge is the ambiguity in both the sign and magnitude of the slope in photo-intensity as a function of speckle displacement. If the signals are corrected so that every element has the same phase (i.e., all elements are made to have a positive slope), then the weighted average shows an increase in signal to noise ratio as the number of elements is increased.

A demonstration of the power of arrays for improving signal-to-noise was made by comparing the signals of individual detector elements with a phase-corrected average of 18 combined elements. The 18 independent signals were obtained by using a three-element array to monitor six different random speckle patterns, each undergoing the same displacement. The SNR of the phase-corrected average was superior by approximately 10 dB over the typical single element signal. In this demonstration case, the phases were sorted manually during post processing.

7. Conclusions

This chapter has shown how photoconductive detectors tens of microns in size can provide more sensitivity than photo-diodes. Very small photo-diodes have very small areas, which limits their sensitivity at high bandwidth. They are useful in applications such as single-mode fiber optics telecommunications, because the light is concentrated to a very small area. When signals are as small as a nanowatts, photo-multipliers are often used. However, in applications where spatial resolution at high bandwidth is required, such as monitoring mechanical vibrations, photoconductive elements can have the best useful figure of merit. We have demonstrated a minimum detectable power of P_{min} is 2 pW•$Hz^{1/2}$.

Experiments showed the most sensitivity with photoconductive GaAs mesas, but speed was limited to tens of kHz because of slow space-charge buildup in regions of sharp transition between light and dark. Reducing the shadows with transparent ITO contacts and reducing the background resistivity with continuous illumination with an LED, provided a response time of about 10 μs, three times faster than without these special measures. Nonetheless, GaAs mesas were unable to respond fast enough to measure ultrasonic waves.

The solution was to use photoconductive mesas in silicon, which does not suffer from space charge buildup. Because carriers can diffuse very far in silicon, it is important to use silicon-on-insulator (SOI) technology, to remove any diffusion into the substrate. It is also necessary to electrically isolate mesas by etching all the way through the silicon layer. With careful etching, mesas 15 μm wide were etched and contacted on either side. These photoconducting mesas were demonstrated to respond in 2 MHz with a 10V bias. Analysis of speckle motion measured with these SOI mesas indicated a sensitivity of δ_{min} = 16 pm $Hz^{1/2}$ W.

Preliminary experiments were carried out to demonstrate improvements when arrays of photo-conducting mesas are used, as long as the signals are properly combined. Further work on arrays will enable system calibration as well as measurement. All results, both experimental and theoretical, indicate chapter that this technology is certainly amenable to further development in practical applications of vibration and motion sensing, particularly at high speeds and small distances.

8. References

Bessette, J. & Garmire, E. (2010). Silicon-on-insulator photoconducting mesas for high-speed detection of laser speckle motion. *Journal of Selected Topics in Quantum Electronics*, Vol. 16, No. 1, Jan/Feb 2010, pp. 93-99.

Bessette, J., Gogo, A. & Garmire, E. (2006). Four-point photo-conductance monitoring array for speckle and fringe motion sensing. *Proceedings of SPIE* , Vol. 6379, Oct 2006, pp. 637903(1-10).

Biswas, K., Das, S. & Kal, S. (2006). Analysis and prevention of convex corner undercutting in bulk micromachined silicon microstructures. *Microelectronics Journal*, Vol. 37, No. 8, Aug 2006, pp. 765-769.

Brodeur, P.H., Johnson, M.A., Berthelot, Y.H. & Gerhardstein, J.P. (1997). Noncontact laser generation and detection of Lamb waves in paper. *Journal of Pulp and Paper Science*, Vol. 23, No. 5, May 1997, pp. J238-J243.

Bube, R.H. (Ed) (1960). *Photoconductivity of Solids*. John Wiley & Sons, Library of Congress Control Number lc60010309, New York, 1960.

Burm, J. & Eastman, L.F. (1996). Low-frequency gain in MSM photodiodes due to charge accumulation and image force lowering. *IEEE Photonics Technology Letters*, Vol. 38, No. 1, Jan 1996, pp. 113-115.

Carrano, J.C., Li, T., Grudowski, P.A., Eiting, C.J., Dupuis, R.D. & Campbell, J.C. (1998). Comprehensive characterization of metal-semiconductor-metal ultraviolet photodetectors fabricated on a single-crystal GaN. *Journal of Applied Physics*, Vol. 83, No. 11, June 1998, pp. 6148-6160.

Celler, G.K. & Cristoloveanu, S. (2003). Frontiers of silicon on insulator. *Journal of Applied Physics*, Vol. 93, No. 9, May 2003, pp. 4955-4978.

Cheeke, J.D.N. (2002). *Fundamentals and Applications of Ultrasonic Waves*. CRC Press, ISBN 0-8493-0130-0, Boca Raton, Florida.

Cofaru, C., Philips, W. & Van Paepegem, W. (2010). Evaluation of digital image correlation techniques using realistic ground truth speckle images. *Measurement Science and Technology*, Vol. 21, No. 5, March 2010, 055102 (17pp).

Dainty, J.C. (ed)(1975). *Topics in Applied Physics. Vol. 9, Laser Speckle and Related Phenomena*, Springer-Verlag, ISBN 0387131698, 9780387131696, Berlin and New York.

Davies, S.J., Edwards, C., Taylor, G. S. & Palmer, S. B. (1993). Laser-generated ultrasound: its properties, mechanisms and multifarious applications. *Journal of Physics D: Applied Physics*, Vol. 26, No. 3, Nov 1993, pp. 329-348.

Heinz, P. (2008). *Optical Vibration Detection with a Four-Point Photoconductance-Monitoring Array*. Ph.D. thesis, Thayer School of Engineering at Dartmouth College, 2008.

Heinz, P. & Garmire, E. (2004). Optical vibration detection with a photoconductance monitoring array. *Applied Physical Letters*, Vol. 84, No. 16, April 2004, pp. 3196–3198.

Heinz, P. & Garmire, E. (2005) Low-power optical vibration detection by photoconductance-monitoring with a laser speckle pattern. *Optics Letters*, Vol. 30, No. 22, Nov 2005, pp. 3027–3029.

Heinz, P. & Garmire, E. (2007). Photoconductive arrays for monitoring motion of spatial optical intensity patterns. *Applied Optics*, Vol. 46, No. 35, Dec 2007, pp. 8515–8526.

Jhang, K.Y., Shin, M.J. & Lim, B.O. (2006). Application of the laser generated focused Lamb wave for non-contact imaging of defects in plate. *Ultrasonics*, Vol. 44, No. 1, Dec 2006, pp. e1265-e1268.

Kamshilin, A., Miridonov, S.V., Sidorov, I.S., Semenov, D.V. & Nippolainen, E. (2009). Statistics of dynamic speckles in application to distance measurements. *Optical Review*, Vol. 16, No. 2, March 2009, pp. 160-166.

Komatsu, S., Yamaguchi, I. & Saito, H. (1976). Velocity measurement using structural change of speckle. *Optics Communications*, Vol. 18, No. 3, Aug 1976, pp. 314-316.

Lee, D.B. (1969). Anisotropic etching of silicon. *Journal of Applied Physics*, Vol. 40, No. 11, Oct 1969, pp. 4569-4574.

Liu, J.M. (2005). *Photonic Devices*. Cambridge University Press, ISBN: 9780521551953, UK, 2005-04-21.

Lowe, M.J.S. & Diligent, O. (2002). Low-frequency reflection characteristics of the S_0 Lamb wave from a rectangular notch in a plate. *Journal of the Acoustical Society of America*, Vol. 111, No. 1, Jan 2002, pp. 64-74.

Macdonald, D., Sinton, R.A. & Cuevas, A. (2001). On the use of a bias-light correction for trapping effects in photoconductance-based lifetime measurements of silicon. *Journal of Applied Physics*, Vol. 89, No. 5, March 2001, pp. 2772-2778.

Mendicino, M.A. (1999), in *Properties of Crystalline Silicon*. Hull, R. (ed.) (1999), The Institution of Electrical Engineers, ISBN: 0852969333, London, UK, 1999.

Monchalin, J.P. (2007). Laser-Ultrasonics: Principles and Industrial Applications, chapter 4, in: *Ultrasonic and Advanced Techniques for Nondestructive Testing and Material Characterization*, C.H. Chen (Ed), pp. 79-116, World Scientific Publishing Co., ISBN: 978-981-270-409-2, Singapore.

Neamen, D. (2003). *Semiconductor Physics and Devices*, McGraw-Hill, ISBN: 0072321075, New York.

Pei, J., Degertekin, F.L., Khuri-Yakub, B.T. & Saraswat, K.C. (1995). *In situ* thin film thickness measurement with acoustic Lamb waves. *Applied Physics Letters*, Vol. 66, No. 17, April 1995, pp. 2177-2179.

Pierce, S.G., Culshaw, B. & Shan, Q. (1998). Laser generation of ultrasound using a modulated continuous wave laser diode. *Applied Physics Letters*, Vol. 72, No. 9, March 1998, pp. 1030-1032.

Rong, H., Liu, A., Nicolaescu, R. & Paniccia, M. (2004). Raman gain and nonlinear optical absorption measurements in a low-loss-silicon waveguide. *Applied Physics Letters*, Vol. 85, No. 12, Sept 2004, pp. 2196-2198.

Rose, A. (1955). Space-charge-limited currents in solids. *Physical Review*, Vol. 97, No. 6, March 1955, pp.1538-1544.

Rose, A. & Lampert, M.A. (1959). Photoconductor performance, space-charge currents, and the steady-state Fermi level. *Physical Review*, Vol. 113, No. 5, March 1959, pp. 1227-1235.

Scruby, C.B. & Drain, L.E. (1990). *Laser ultrasonics: techniques and applications*. CRC Press, ISBN 0750300507, New York.

Soares, S.F. (1992). Photoconductive gain in a Schottky barrier photodiode. *Japanese Journal of Applied Physics*, Vol. 31, No. 2A, Feb 1992, pp. 210-216.

Sze, S.M. & Ng, K.K. (2007). *Physics of Semiconductor Devices, 3rd Ed.* John Wiley & Sons, ISBN: 978-0-471-14323-9, New York, 2007.

Tu, S.L. & Baliga, B.J. (1992). On the reverse blocking characteristics of Schottky power diodes. *IEEE Tranactions on Electron Devices*, Vol. 39, No. 12, Dec 1992, pp. 2813-2814.

Wu, X.P. & Ko, W.H. (1989). Compensating corner undercutting in anisotropic etching of (100) silicon. *Sensors and Actuators*, Vol. 18, No. 2, June 1989, pp. 207-215.

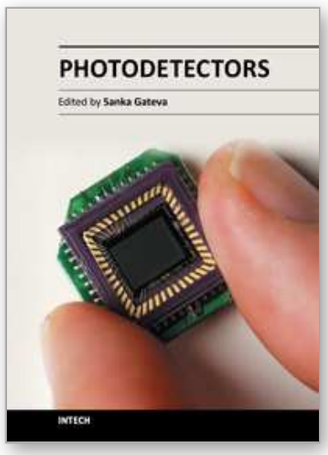

Photodetectors

Edited by Dr. Sanka Gateva

ISBN 978-953-51-0358-5
Hard cover, 460 pages
Publisher InTech
Published online 23, March, 2012
Published in print edition March, 2012

In this book some recent advances in development of photodetectors and photodetection systems for specific applications are included. In the first section of the book nine different types of photodetectors and their characteristics are presented. Next, some theoretical aspects and simulations are discussed. The last eight chapters are devoted to the development of photodetection systems for imaging, particle size analysis, transfers of time, measurement of vibrations, magnetic field, polarization of light, and particle energy. The book is addressed to students, engineers, and researchers working in the field of photonics and advanced technologies.

How to reference

In order to correctly reference this scholarly work, feel free to copy and paste the following:

Jonathan Bessette and Elsa Garmire (2012). Photoconductors for Measuring Speckle Motion to Monitor Ultrasonic Vibrations, Photodetectors, Dr. Sanka Gateva (Ed.), ISBN: 978-953-51-0358-5, InTech, Available from: http://www.intechopen.com/books/photodetectors/photoconductor-arrays-for-non-contact-sensing-of-motion

INTECH
open science | open minds

InTech Europe
University Campus STeP Ri
Slavka Krautzeka 83/A
51000 Rijeka, Croatia
Phone: +385 (51) 770 447
Fax: +385 (51) 686 166
www.intechopen.com

InTech China
Unit 405, Office Block, Hotel Equatorial Shanghai
No.65, Yan An Road (West), Shanghai, 200040, China
中国上海市延安西路65号上海国际贵都大饭店办公楼405单元
Phone: +86-21-62489820
Fax: +86-21-62489821

IntechOpen